Entangled Impacts of Large-Scale Monsoon Flows and Terrain Circulations on the Diurnal Cycle of Rainfall over the Himalayas

AOQI ZHANG,[a] YILUN CHEN,[a] XIAO PAN,[b] SHUMIN CHEN,[a] WEIBIAO LI,[a] AND YUNFEI FU[c]

[a] *Southern Marine Science and Engineering Guangdong Laboratory (Zhuhai), School of Atmospheric Sciences, Sun Yat-sen University, Zhuhai, Guangdong, China*

[b] *Institute of Atmospheric Environment, China Meteorological Administration, Opening Key Laboratory for Northeast Cold Vortex Research, Shenyang, Liaoning, China*

[c] *School of Earth and Space Sciences, University of Science and Technology of China, Hefei, Anhui, China*

(Manuscript received 7 April 2021, in final form 4 November 2021)

ABSTRACT: The diurnal features of rainfall over the Himalayas have been widely investigated, but their triggers remain unclear. In this work, we divided the Himalayas and surroundings into four regions, including the plains, foothills, slopes, and plateau, and investigated the above issues. The results show that the rainfall total is controlled by large-scale monsoon flows while its meridional distribution is regulated by terrain circulations. The afternoon rainfall peak in the plains and foothills is linked with the intersection of two monsoon flows. The southward-shifting rainfall peak, which occurs from midnight to early morning in the slopes and foothills, is affected by the nighttime downslope flow and the strong Bay of Bengal monsoon flow in the morning. The evening rainfall peak in the plateau and high-altitude slopes is thought to be a result of the atmospheric layer being at its moistest at that time.

SIGNIFICANCE STATEMENT: During the South Asian summer monsoon season, the Himalayas are affected by two large-scale monsoon flows as well as unique topographic circulations. We want to understand how these complex circulations act on diurnal variations of orographic precipitation. The diurnal cycle of rainfall over the Himalayas and surroundings shows three prominent south-to-north peaks, which are caused by significantly different thermodynamic conditions. The southward-shifting diurnal rainfall peak over the Himalayan slopes and foothills, which contributes the most to the arc-shaped orographic rain belt, is triggered by the nighttime downslope flow and strengthened by the strong Bay of Bengal monsoon flow in the morning. The result highlights the entangled impact of monsoon and terrain circulations on orographic precipitation.

KEYWORDS: Complex terrain; Orographic effects; Monsoons; Rainfall

1. Introduction

Orographic precipitation has regional, seasonal, and complex characteristics, and plays an important role in the global water cycle and energy budget (Kingsmill et al. 2016; Kumar et al. 2019). The Himalayas are the highest mountain range in the world, characterized by dramatic variations in altitude at its southern slopes, and has long been a key area for research on topographic precipitation (Gadgil and Sajani 1998; Fu et al. 2018). During the South Asian summer monsoon season, two large-scale monsoon flows—from the Bay of Bengal (BOB) and the Arabian Sea, respectively—travel toward the Himalayas, forming a unique arc-shaped precipitation belt near the Himalayas (Bhatt and Nakamura 2005; Pang et al. 2012). Under the influence of heavy precipitation, major disasters such as floods and mudslides occur frequently over this region, causing severe economic losses and human casualties (Rasmussen and Houze 2012).

Benefiting from the development of observational methods and numerical models in the past 20 years, much progress has been made in the study of precipitation over the Himalayas. However, there is continued debate regarding the dominant trigger of the Himalayan rain belt. Wu et al. (2007) proposed that it is the summertime "heat pump" effect of the Tibetan Plateau, which drives local ascent and causes low-level moist air to converge over the Tibetan Plateau, while Boos and Kuang (2010) argued the mechanical isolation of the Himalayas is the key factor. Moreover, the mountain–valley wind circulation and local thermal forcing can also be triggers of precipitation over the Himalayas (Houze et al. 2007; Wang et al. 2016). In terms of the features of precipitation, Bookhagen and Burbank (2006) pointed out the existence of two distinct rainfall peaks, at elevations of around 0.9 and 2.1 km, respectively, based on 8-yr Tropical Rainfall Measuring Mission (TRMM) Precipitation Radar (PR) observations. Shrestha et al. (2012) further revealed that the former rain peak is attributed to fewer heavy rainfall events while the latter is caused by frequent, weak, but persistent rainfall events. This is because the frequency of precipitation increases while the intensity of rainfall decreases with increasing altitude over the Himalayas (Fu et al. 2018). By analyzing the surface wind of precipitation systems,

Supplemental information related to this paper is available at the Journals Online website: https://doi.org/10.1175/10.1175/jas-d-21-0111.s1.

Corresponding authors: Yilun Chen, chenylun3@mail.sysu.edu.cn; Weibiao Li, esslwb@mail.sysu.edu.cn

DOI: 10.1175/JAS-D-21-0111.1

© 2022 American Meteorological Society. For information regarding reuse of this content and general copyright information, consult the AMS Copyright Policy (www.ametsoc.org/PUBSReuseLicenses).

Brought to you by Sun Yat-Sen University | Unauthenticated | Downloaded 02/12/22 10:21 AM UTC

Zhang et al. (2018) further explored the impact of various precipitation mechanisms on the structures of Himalayan precipitation.

Diurnal variation is an important aspect of precipitation research. In land areas, late afternoon is usually the peak time of precipitation because of the surface heating (Nesbitt and Zipser 2003; Yu et al. 2014). However, this conclusion is not always applicable. For instance, controlled by the sea–land breeze circulation, coastal regions often present a morning peak (Johnson 2011; Chen et al. 2018). During summertime, the diurnal cycle of rainfall in the Yangtze River basin shows obvious eastward propagation, characterized by a midnight peak in the upper reaches, an early morning peak in the middle reaches, and an afternoon peak in the lower reaches, which may be linked with the eastward movement of cloud systems from the Tibetan Plateau (Yu et al. 2007). The diurnal variation of mei-yu precipitation over the Yangtze Plain appears as a unique morning peak in normal mei-yu years (Xue et al. 2018), whereas it shows two diurnal peaks—one in the morning and one in the afternoon—in atypical mei-yu years, such as 2018 (Zhang et al. 2020).

Generally, under the influence of the mountain–valley wind circulation, orographic precipitation peaks in the afternoon over slopes, but in the early morning over valleys (Barros et al. 2000). Using TRMM 3B42 data on $0.25° \times 0.25°$ grids with a time interval of 3 h, Sahany et al. (2010) found that the rainfall diurnal cycle peaked at midnight in the foothills of the Himalayas. Pan et al. (2021) used multiyear TRMM PR 2A25 data to further point out two distinct rainfall peaks—one in the afternoon and one at midnight—over the slopes of the Himalayas. By using spatiotemporal TRMM PR and ERA5 data, Fujinami et al. (2021) also revealed the double peaks and suggested that the upslope flow drives the daytime peak and the monsoon nocturnal jet creates the nighttime peak. Based on a combination of JRA-55 and TRMM 3B42 data, Chen (2020) proposed that the nocturnal speedup of the summer monsoon (nocturnal jet) is key for the nighttime rainfall peak around the Himalayas, and the location of the Himalayan rain belt is regulated by both the background monsoon intensity and its diurnal amplitude.

Previous studies have summarized the features of rainfall diurnal variations over the Himalayas well. However, the physical triggers for the diurnal variations of rainfall remain unclear owing to the low temporal resolution of environmental data. Specifically, during the summer monsoon season, the Himalayas are affected by two large-scale monsoon flows, as well as unique topographic circulations, and more attention needs to be paid to how these complex circulation conditions affect diurnal cycles of rainfall over the Himalayas.

In this paper, we use the Integrated Multisatellite Retrievals for GPM (IMERG) half-hourly precipitation product and ERA5 hourly reanalysis data to conduct in-depth analysis on the above issues. After introducing the data and methods employed in this study in the next section, the main body of this work is presented in section 3 and comprises two aspects. First, the sensitivity of the distribution of precipitation over the Himalayas to various circulation intensities is tested in section 3a. And second, the diurnal variation of precipitation over the Himalayas and its relevant triggers are further discussed in section 3b. Conclusions and a summary are provided in the final section.

2. Data and methods

As a continuation of previous work, we followed the regional division used in Chen et al. (2017). Since the topography of the Himalayas and its southern rain belt are arc shaped, we divided the Himalayas and surrounding areas into four regions by concentric arcs (Fig. 1). The four regions are the flat Gangetic Plains (plains), the foothills of the Himalayas (foothills), the steep slopes of the Himalayas (slopes), and the Himalayan–Tibetan Plateau tableland (plateau). The study period is that of the summer monsoon season (June–September) from 2014 to 2018.

We used IMERG version 6 precipitation data provided by the Precipitation Measurement Mission website (https://pmm.nasa.gov). IMERG combines the precipitation retrievals from multiple satellite microwave- and infrared-based instruments as well as rainfall measurements from ground-based rain gauges, providing half-hourly rain rates on $0.1° \times 0.1°$ grids (Huffman et al. 2019). According to the calculation time and usage data, IMERG is subdivided into three products—namely, "early run," "late run," and "final run." The IMERG "final run" product was used in this study.

Tan et al. (2019) compared precipitation diurnal cycle derived from IMERG and ground measurements over different regions around the globe, and suggested a slight lag in the diurnal phase of only +0.59 h. However, the quality index of IMERG is low over the Himalayas and Tibetan Plateau due to discarded microwave estimates (Huffman et al. 2020). In other words, IMERG estimates are highly sensitive to information from infrared data over there. Note that there are more high-level cirrus clouds over the Himalayas during nighttime (Chen et al. 2017), IMERG may underestimate the proportion of daytime precipitation over the slopes and Tibetan Plateau. In addition, the estimate threshold employed in IMERG is about 0.03 mm h^{-1} (Huffman et al. 2020), which is smaller than the minimum detectable rain rate of GPM 2ADPR (about 0.2 mm h^{-1}) and TRMM PR (about 0.7 mm h^{-1}). At higher altitudes of the slopes and Tibetan Plateau, the rain rate can be weak due to low water-vapor conditions. Thus, higher rainfall rates are estimated by IMERG in areas above 3000 m MSL than those estimated by TRMM PR, especially during nighttime (Fujinami et al. 2021).

We therefore compared the precipitation diurnal variations derived from IMERG and rain gauge data of nine stations in the east portion of the slopes (Figs. S1 and S2 in the online supplementary file). The results are consistent with Ouyang et al. (2020) that IMERG data generally reproduce both the afternoon and nighttime peaks observed from the rain gauges. Thus, IMERG data are still applicable for

Brought to you by Sun Yat-Sen University | Unauthenticated | Downloaded 02/12/22 10:21 AM UTC

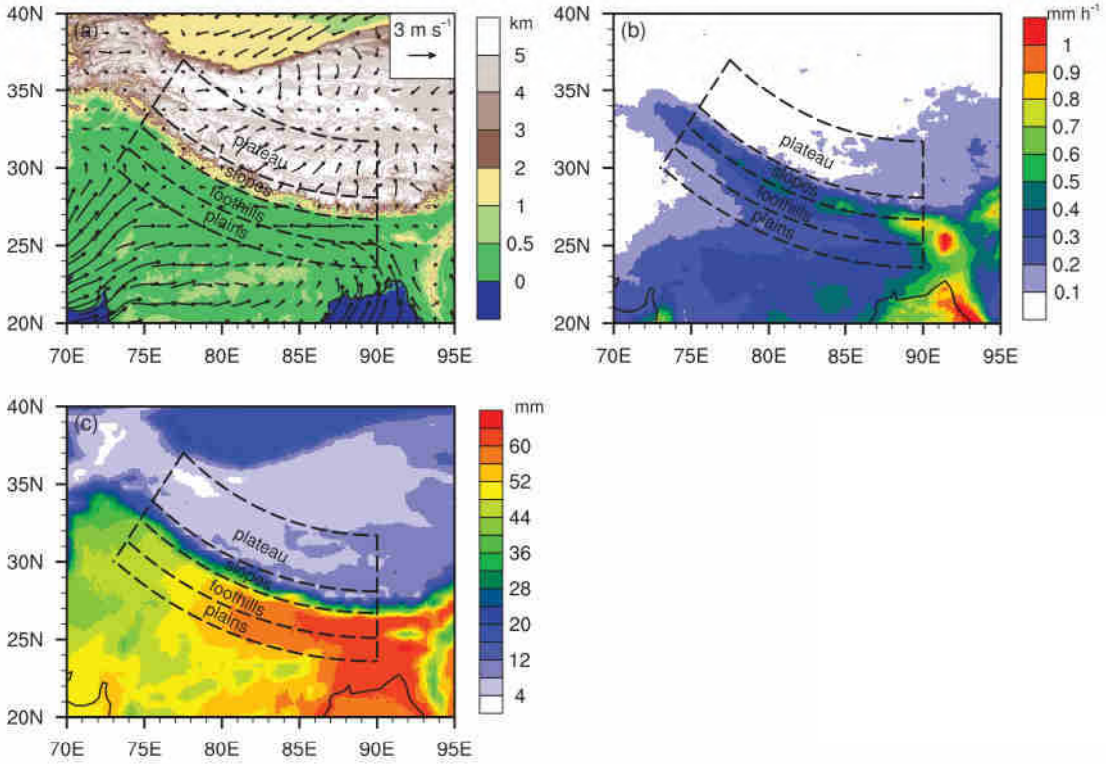

FIG. 1. Horizontal distributions of (a) terrain height overlapped with average 10-m winds derived from ERA5, (b) average near-surface rain rate, including nonprecipitation grid cells, derived from IMERG, and (c) the average total column water vapor derived from GPM 2AGPROFGMI for June–September 2014–18. The dashed lines and arcs indicate our study regions.

revealing the diurnal variations of precipitation over the Himalayas.

In addition, we also used the total column water vapor information from the Global Precipitation Mission (GPM) 2AGPROFGMI product. The wind, specific humidity, geopotential, and other environmental data used in this study were provided by ERA5, which is the latest generation of reanalysis data produced by the European Centre for Medium-Range Weather Forecasts (Hersbach et al. 2020). ERA5 data are provided on 0.25° × 0.25° grids with 37 vertical levels and a temporal interval of 1 h, which can well meet the needs of research on diurnal variation of precipitation.

Figure 1 shows the horizontal distributions of topography, near-surface flow at 10 m above ground level, rain rate, and precipitable water over the study region. The average near-surface airflow in the slopes appears as upslope flow, while that in the foothills appears as easterly circumfluent flow (Fig. 1a). The horizontal distribution of average rain rate from IMERG shows consistency with previous studies, which are derived from TRMM PR (Bookhagen and Burbank 2006; Shrestha et al. 2012) and GPM Dual-Frequency Precipitation Radar (DPR) (Zhang et al. 2018). The arc-shaped rain belt is mainly located in the slopes and foothills (Fig. 1b). Due to the difference in terrain height, the average precipitable water in the four regions presents a stepped distribution (Fig. 1c). In addition, the average precipitable water, as well as the near-surface rain rate, are higher in the east portion of the study region than in the west, indicating the monsoon flow from the BOB is much moister than that from the Arabian Sea.

Since the near-surface airflow direction in the slopes is dominated by slope flow while that in the foothills is mainly circumfluent flow (Zhang et al. 2018; Pan et al. 2021), the average slope wind speed of the slopes (F_{slope}) and average circumfluent wind speed of the foothills (F_{foothill}) were defined as follows:

$$F_{\text{foothill}} = \frac{1}{N_{\text{slope}}} \sum_{i=1}^{N_{\text{slope}}} (U_i \cos\,\theta + V_i \sin\,\theta), \tag{1}$$

$$F_{\text{foothill}} = \frac{1}{N_{\text{foothill}}} \sum_{i=1}^{N_{\text{foothill}}} (-U_i \sin\,\theta + V_i \cos\,\theta), \tag{2}$$

where N_{slope} and N_{foothill} represent the total grid number of the ERA5 data within the slopes and foothills, respectively; the subscript "i" stand for different ERA5 grid in the study region; U and V are the zonal and meridional components of near-surface flow, respectively; and θ indicates the angle between the eastward direction and the direction of ERA5 grid cell to the concentric arc center ($0 < \theta \le 0.5\pi$ within the study region). A positive F_{slope} indicates upslope flow in the

Brought to you by Sun Yat-Sen University | Unauthenticated | Downloaded 02/12/22 10:21 AM UTC

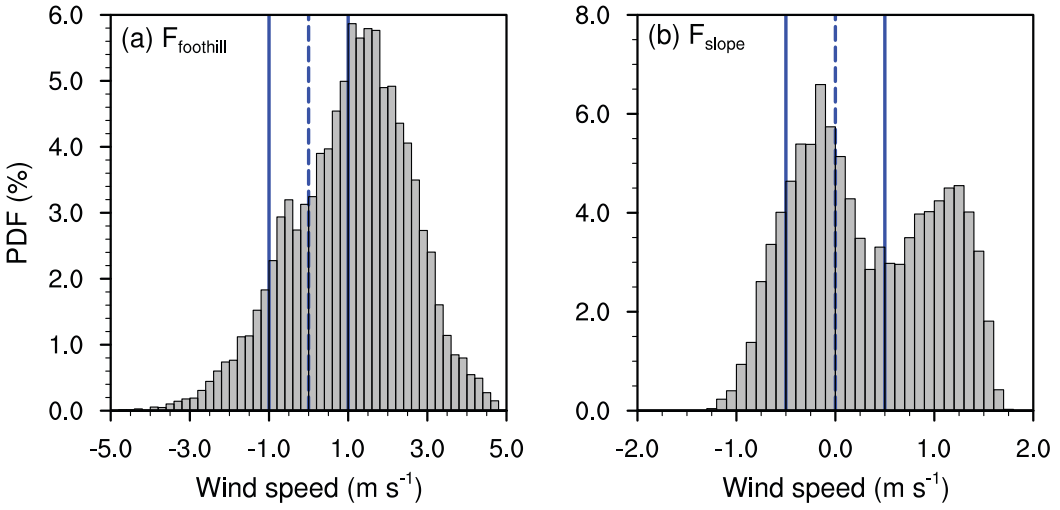

FIG. 2. PDFs of (a) average circumfluent flow over the foothills ($F_{foothill}$) and (b) average slope flow over the slopes (F_{slope}), derived from ERA5 data for June–September 2014–18. The intervals on the x axis are 0.2 and 0.1 m s^{-1} for (a) and (b), respectively. The solid blue lines indicate the thresholds for classification, while the dash blue lines indicate the wind speed of 0 m s^{-1}.

slopes, whereas a positive $F_{foothill}$ indicates easterly circumfluent flow in the foothills.

3. Results

a. *Sensitivity of precipitation to near-surface flow*

The sensitivity experiment, which involves studying the relationship between two parameters while controlling other variables, is an important method in scientific research (Wang et al. 2019). In this section, we focus on the sensitivity of the precipitation distribution over the Himalayas to the two types of near-surface flow through classification and statistics.

First, the probability distribution functions (PDFs) of $F_{foothill}$ and F_{slope} are given in Fig. 2. Figure 2 shows that $F_{foothill}$ is mainly distributed in the interval of −4 to 5 m s^{-1} (Fig. 2a). The PDF of $F_{foothill}$ presents a unimodal distribution with a peak at 1.5 m s^{-1}, which indicates that the average circumfluent flow in the Himalayan foothills is about 1.5 m s^{-1} from the east. We used 1 and −1 m s^{-1} as thresholds to classify $F_{foothill}$ into three categories: westerly circumfluent, weak flow, and easterly circumfluent. The sample sizes of the three classes of $F_{foothill}$ account for 9.2%, 34.9%, and 55.8%, respectively, of all samples. This indicates that the easterly monsoon flow from the BOB is the main source of near-surface flow in the foothills.

The F_{slope} is mainly distributed in the interval of −1.2 to 1.7 m s^{-1}, indicating that the average slope flow in the slopes is usually between −1.2 (downslope flow) and 1.7 m s^{-1} (upslope flow) (Fig. 2b). The PDF of F_{slope} shows a bimodal structure with peaks at −0.15 and 1.35 m s^{-1}. Similarly, we used −0.5 and 0.5 m s^{-1} as thresholds and divided F_{slope} into three classes: downslope flow, weak flow, and upslope flow. These classes account for 13.0%, 46.8%, and 40.2%, respectively, of all samples.

Figure 3 shows the horizontal distributions of near-surface flow and rain rate for different classes of $F_{foothill}$. The Student's t test values of rain rate differences between any $F_{foothill}$ class and the other samples exceeds 2 in the west-to-middle portion of the study region (Fig. S3), indicating robust statistical differences (p value > 95%) of average rain rates there. Since the samples are categorized according to the ERA5 10-m winds, the significance levels of wind field differences are higher than that of precipitation rate (Fig. S4). When $F_{foothill}$ shows as easterly flow, the BOB monsoon flow is strong and dominates the foothills and plains (Fig. 3a). At this time, precipitation is distributed relatively uniformly from east to west in the study region, and the highest near-surface rain rate occurs at the junction of the foothills and slopes with a value of ~0.6 mm h^{-1} (Fig. 3b). When $F_{foothill}$ appears as weak flow, the west portion of the foothills and plains is controlled by the Arabian Sea monsoon flow, while the east portion is dominated by the BOB monsoon flow (Fig. 3c). The two flows converge at about 85°E, forming a weak convergence field there. At this time, the near-surface rain rate in the west portion of the study area decreases significantly, whereas the near-surface rain rate in the east increases slightly with a value of 0.8 mm h^{-1} (Fig. 3d). When $F_{foothill}$ shows as westerly flow, the middle and west portion of the foothills and plains are dominated by a strong Arabian Sea monsoon flow, while the BOB monsoon flow is weak in the east (Fig. 3e). The average precipitation is the weakest among all types of $F_{foothill}$ (Fig. 3f), with a near-surface rain rate of less than 0.1 mm h^{-1} in most regions except the east portion of the foothills and plains. The precipitation is concentrated to the east of the study region with a peak near-surface rain rate exceeding 1 mm h^{-1}.

Similarly, Fig. 4 shows the horizontal distribution of near-surface flow and rain rate for different classes of F_{slope}. The Student's t test showed that the rain rate differences between F_{slope} classes and the other samples are significant in the

Brought to you by Sun Yat-Sen University | Unauthenticated | Downloaded 02/12/22 10:21 AM UTC

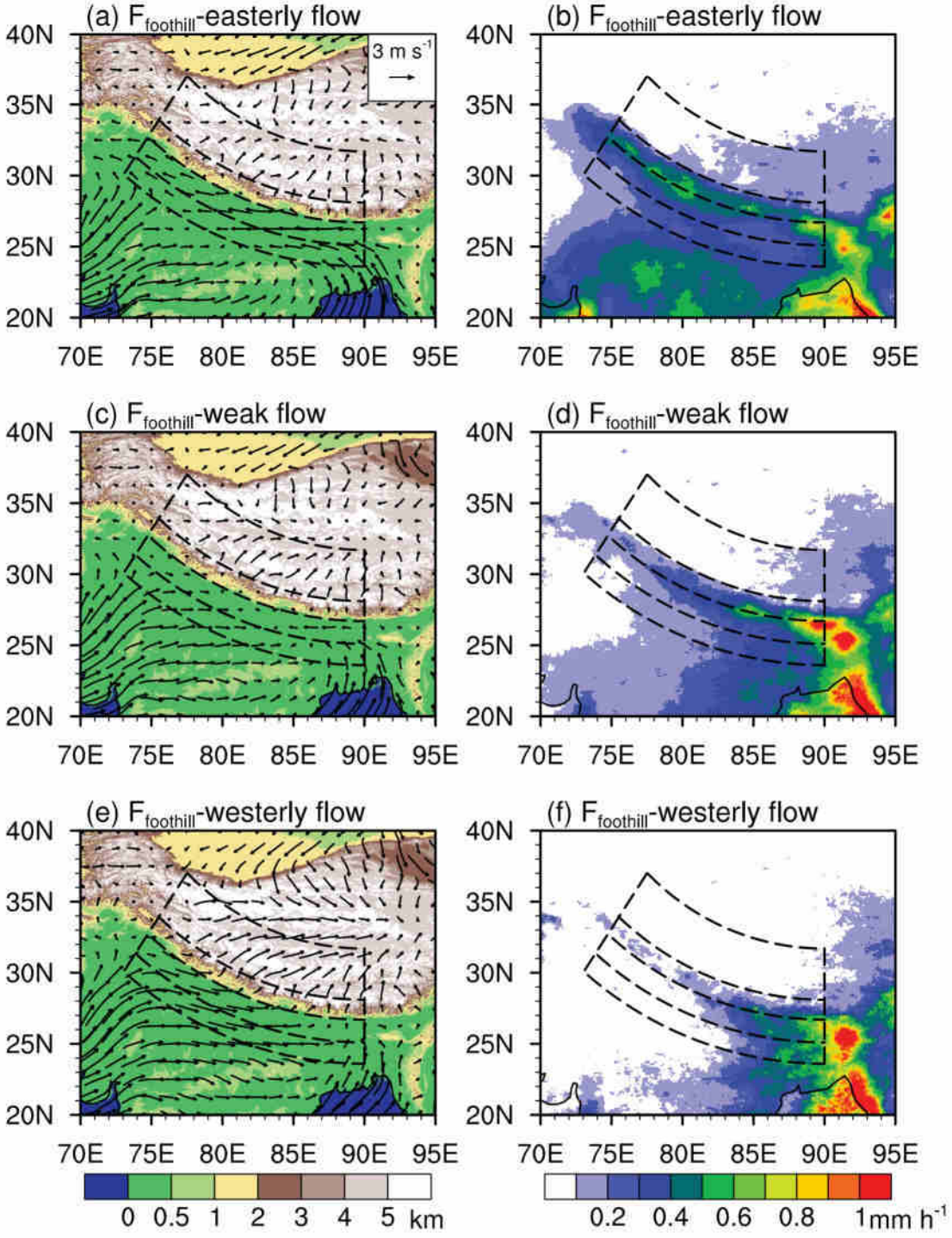

FIG. 3. (a),(c),(e) Horizontal distributions of terrain height overlapped with ERA5 10-m winds and (b),(d),(f) IMERG near-surface rain rate for different classes of $F_{foothill}$.

slopes and northern foothills (Fig. S3). For the upslope F_{slope} class, precipitation is distributed quite uniformly in the study region with an average near-surface rain rate of ~0.3 mm h^{-1} (Fig. 4b). The arc-shaped rain belt at the boundary of the slopes and foothills is insignificant. For the weak F_{slope} class, the average rainfall intensity is strongest, with a significant arc-shaped rain belt (Fig. 4d), which is different from the traditional mountain–valley wind circulation where precipitation in the valley often occurs under downslope winds (Yuan et al. 2012). We think it is resulted from the convergence of weak F_{slope} flow and strong BOB monsoon flow (Figs. 7, 9a, and 11a). For the downslope F_{slope} class (Fig. 4f), precipitation is

Brought to you by Sun Yat-Sen University | Unauthenticated | Downloaded 02/12/22 10:21 AM UTC

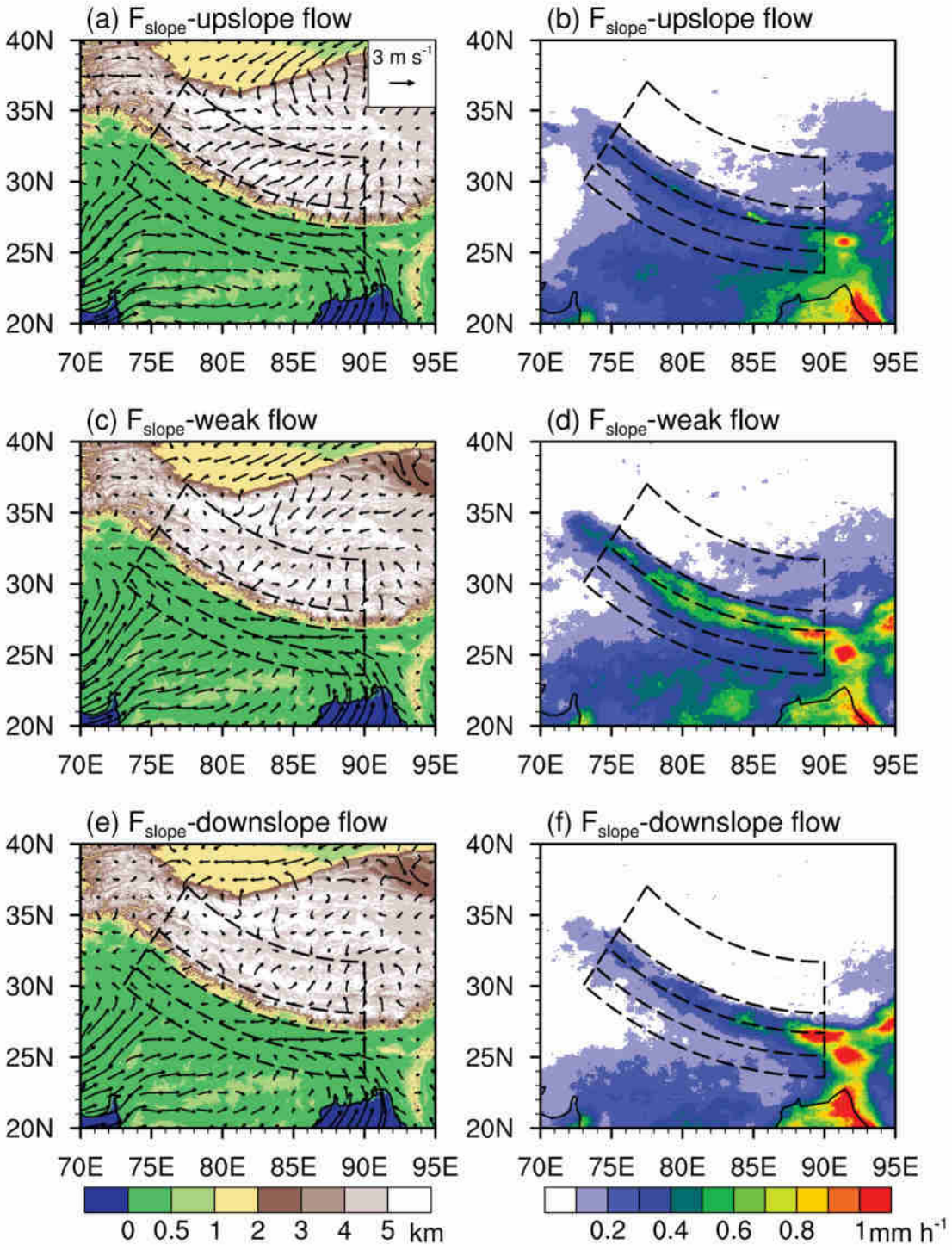

FIG. 4. As in Fig. 3, but for different classes of F_{slope}.

concentrated at the junction of the slopes and foothills; the average near-surface rain rate in the plateau is less than 0.1 mm h^{-1}.

In addition, Figs. 3 and 4 also show that F_{slope} and $F_{foothill}$ are not independent. For instance, when $F_{foothill}$ shows as westerly circumfluent flow, the upslope flow over the slopes is significantly stronger than in the two other classes of $F_{foothill}$ (Figs. 3a,c,e). When F_{slope} appears in the upslope class, the easterly circumfluent flow is the weakest among all F_{slope} classes (Figs. 4a,c,e). The coupling between $F_{foothill}$ and F_{slope} is likely to be the internal cause of the unique diurnal cycle of rainfall over the Himalayas and surrounding areas (Chen 2020).

For a more intuitive understanding of the relationship between rainfall distributions and Himalayan topography, the south-to-north distributions of average rainfall for various

Brought to you by Sun Yat-Sen University | Unauthenticated | Downloaded 02/12/22 10:21 AM UTC

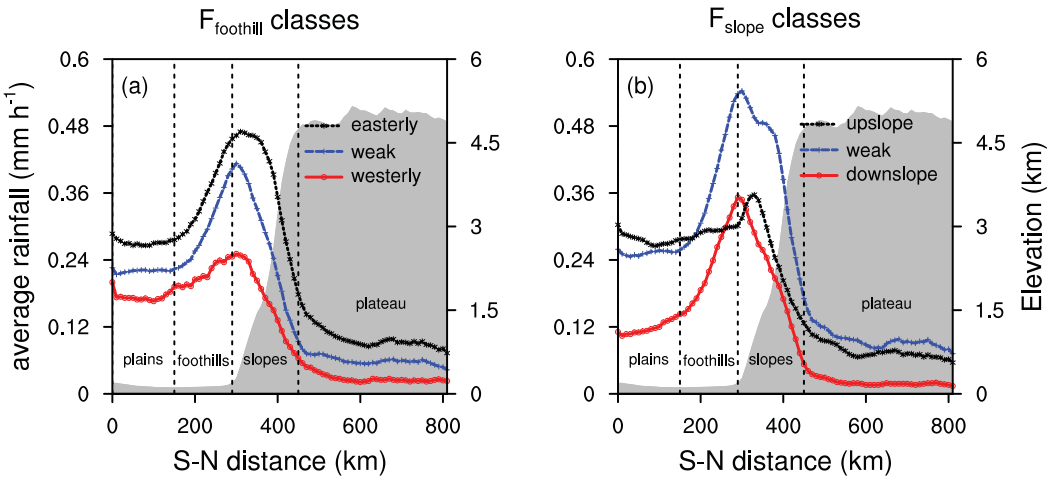

FIG. 5. South-to-north distributions of average rainfall for (a) different F_{foothill} classes and (b) different F_{slope} classes along the south-to-north cross sections of the study region. The shadowed area indicates the relative terrain height.

F_{foothill} and F_{slope} classes are presented in Fig. 5. Specifically, the south-to-north distributions were taken by averaging the IMERG grid cells along the radial of the concentric arcs over the study region. Generally, the south-to-north peak of precipitation occurs at the junction of the foothills and slopes, which is the location of the arc-shaped precipitation belt mentioned above (Fig. 1b). The south-to-north distributions for different F_{foothill} classes are quite similar, except for the values (Fig. 5a). The rainfall peaks are 0.47, 0.41, and 0.25 mm h^{-1} for the easterly circumfluent, weak, and westerly circumfluent classes of F_{foothill}, respectively. Thus, the large-scale monsoon flows mainly affect the total precipitation rather than the meridional distribution of rainfall: when the BOB monsoon flow prevails, the foothills are controlled by easterly moist flow and the total precipitation increases; whereas the opposite is the case when the Arabian Sea monsoon flow prevails.

In terms of F_{slope}, the south-to-north distributions are significantly different among the three classes (Fig. 5b). The average precipitation is generally strongest for the weak flow class, while it is weakest for the downslope class, which resulted from the convergence of weak F_{slope} flow and strong BOB monsoon flow (Figs. 7, 9a, and 11a). However, this order is not always true for each subregion. For instance, the average rain rate of the upslope class is larger than the weak flow class over the plains, and the precipitation of the downslope class is stronger than the upslope class at the boundary of the slopes and foothills. The locations of the south-to-north rainfall peaks also differ: the peak occurs at a lower altitude in the slopes for the upslope class, but at the boundary of the slopes and foothills for the downslope class; while for the weak flow class, the south-to-north distribution peaks at the boundary of the slopes and foothills with a northward extension to the

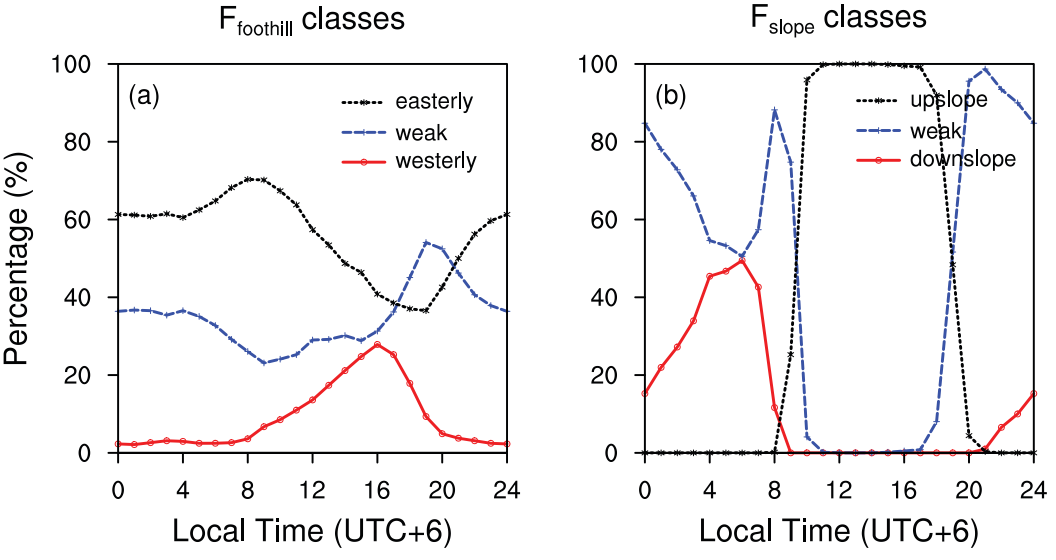

FIG. 6. Diurnal variations of the percentage of different (a) F_{foothill} classes and (b) F_{slope} classes.

Brought to you by Sun Yat-Sen University | Unauthenticated | Downloaded 02/12/22 10:21 AM UTC

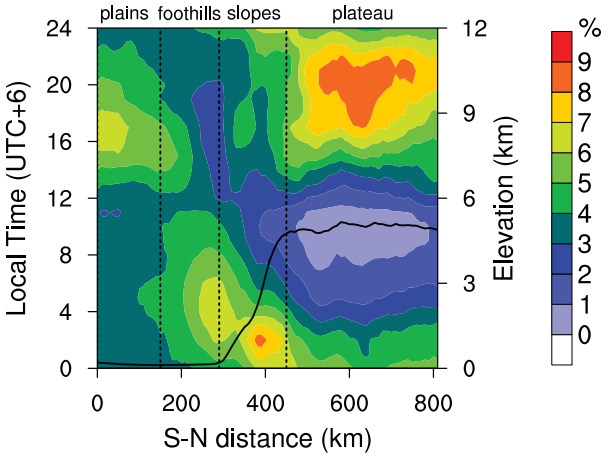

FIG. 7. Diurnal variation of the hourly rainfall percentage along the south-to-north cross section of the study region. The spacings of the *x* axis and *y* axis are 10 km and 1 h, respectively. The dashed lines indicate the boundaries of the study regions. The solid line represents the relative terrain height.

higher altitude of the slopes. These results suggest that the slope winds over the slopes are responsible for the two distinct rainfall peaks at the altitudes of ~0.6 and 2.1 km reported in Bookhagen and Burbank (2006). In addition, as suggested in Fujinami et al. (2021), the IMERG may underestimate afternoon precipitation and hence the average rainfall in case of upslope winds.

In conclusion, the total rainfall amount of the Himalayas is controlled by the large-scale monsoon flows (indicated by F_{foothill}), while the meridional distribution of precipitation is dominated by terrain circulations (indicated by F_{slope}), such as the "heat pump" effect and mountain–valley wind circulations. However, there are still many problems to be solved. For instance, the F_{foothill} can in reality only affect the east–west distributions of moisture and cannot transport moisture to the plateau. Why, then, does the total rainfall amount of the plateau seem to be affected by F_{foothill}? The F_{foothill} and F_{slope} are not independent, so how do they interact with each other to affect precipitation? Considering that F_{slope} is highly dependent on the regional thermal differences and can change drastically within a day, the above issues are investigated from the perspective of diurnal variations in the following section.

Specifically, the diurnal variations of the proportions of the different F_{slope} and F_{foothill} classes are shown in Fig. 6. In terms of the F_{foothill} classes (Fig. 6a), the diurnal variations are mainly caused by the zonal differences of solar heating, which makes the pressure gradient that results in the change of wind directions diurnally. In the morning, as the sun shines directly on the east portion of the study region, the BOB monsoon flow becomes strengthened while the Arabian Sea flow is suppressed; the proportion of the easterly circumfluent class reaches its daily peak of ~70% at 0830 LST (UTC + 6 h). The situation is just the opposite in the afternoon, when the proportion of the westerly circumfluent flow reaches its daily peak of ~30% at 1600 LST. With the weakening of the Arabian Sea monsoon flow and the rebounding of the BOB flow, the proportion of the weak F_{foothill} class reaches its peak of ~55% at 1930 LST.

In terms of the F_{slope} classes (Fig. 6b), the diurnal variations are much more dramatic. From 1000 LST (morning) to 1800 LST (evening), under the summertime "heat pump" effect of the Tibetan Plateau (Wu et al. 2012), the near-surface airflow continuously converges into the Tibetan Plateau region, and F_{slope} always appears as upslope flow. On the other hand, from evening to early morning, when the cooling efficiency of the plateau surface is faster than the upper layer of the plains with the same altitude, the downslope flow gradually increases (Egger et al. 2000). The proportion of the downslope class of F_{slope} reaches its diurnal peak of ~50% at 0600 LST. Influenced by the above two factors, there are two diurnal peaks for the proportion of weak F_{slope}—at around 0800 and 2100 LST, respectively.

b. Diurnal variations

Benefiting from the development of satellite observations, there has been good progress made in understanding rainfall diurnal cycles over the Himalayas (Hirose and Nakamura 2005; Sahany et al. 2010). By using TRMM 2A25 orbital data, Pan et al. (2021) investigated the diurnal variation of rainfall frequency as well as average rainfall intensity along the south-to-north cross section of the study region. Following this work, we adopted IMERG gridded precipitation data with high spatiotemporal resolution and calculated the percentage of hourly rainfall to daily rainfall totals along this same south-to-north cross section (Fig. 7).

The hourly rainfall percentage results are consistent with those of the precipitation frequency or average rainfall intensity (Pan et al. 2021), although IMERG may underestimate the proportion of daytime precipitation over the slopes and Tibetan Plateau. Generally, the diurnal variation of the hourly rainfall percentage shows three major south-to-north centers. In the plateau, as well as the northern slopes, the diurnal rainfall peak appears at about 2000 LST, with the hourly rainfall accounting for more than 9% of the daily rainfall. From the slopes to foothills, there is a clear precipitation peak from midnight to early morning; the peak time gradually transitions from 0200 to 0600 LST, with the hourly rainfall accounting for 6%–8% of the daily rainfall, indicating a southward movement of precipitation from the slopes to the foothills during this period. In the south portion of the foothills and in the plains, the diurnal rainfall peaks at around 1600 LST, with the hourly rainfall accounting for ~5%–7% of the daily total. Specifically, due to the overlapping areas of the three diurnal centers, there are two diurnal rainfall peaks in the south portion of the foothills and in the north portion of the slopes.

Despite numerous investigations into the diurnal features of Himalayan precipitation, the specific triggers for the three diurnal centers of precipitation remain to be revealed. In the following analysis, we use the ERA5 hourly data to analyze

Brought to you by Sun Yat-Sen University | Unauthenticated | Downloaded 02/12/22 10:21 AM UTC

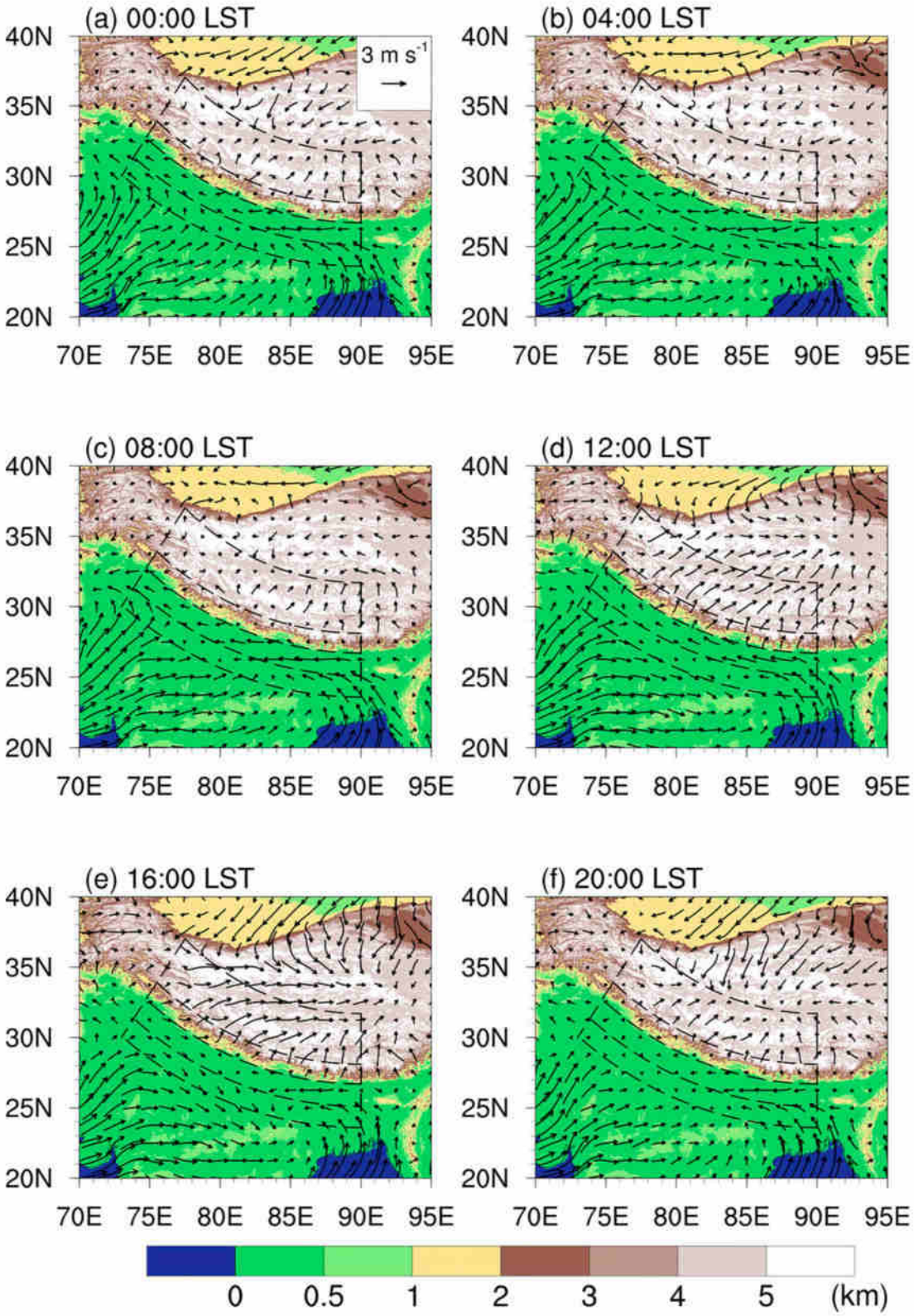

FIG. 8. Horizontal distributions of terrain height overlapped with average ERA5 10-m winds at (a) 0000, (b) 0400, (c) 0800, (d) 1200, (e) 1600, and (f) 2000 LST (UTC + 6 h), derived from ERA5 for June–September 2014–18.

Brought to you by Sun Yat-Sen University | Unauthenticated | Downloaded 02/12/22 10:21 AM UTC

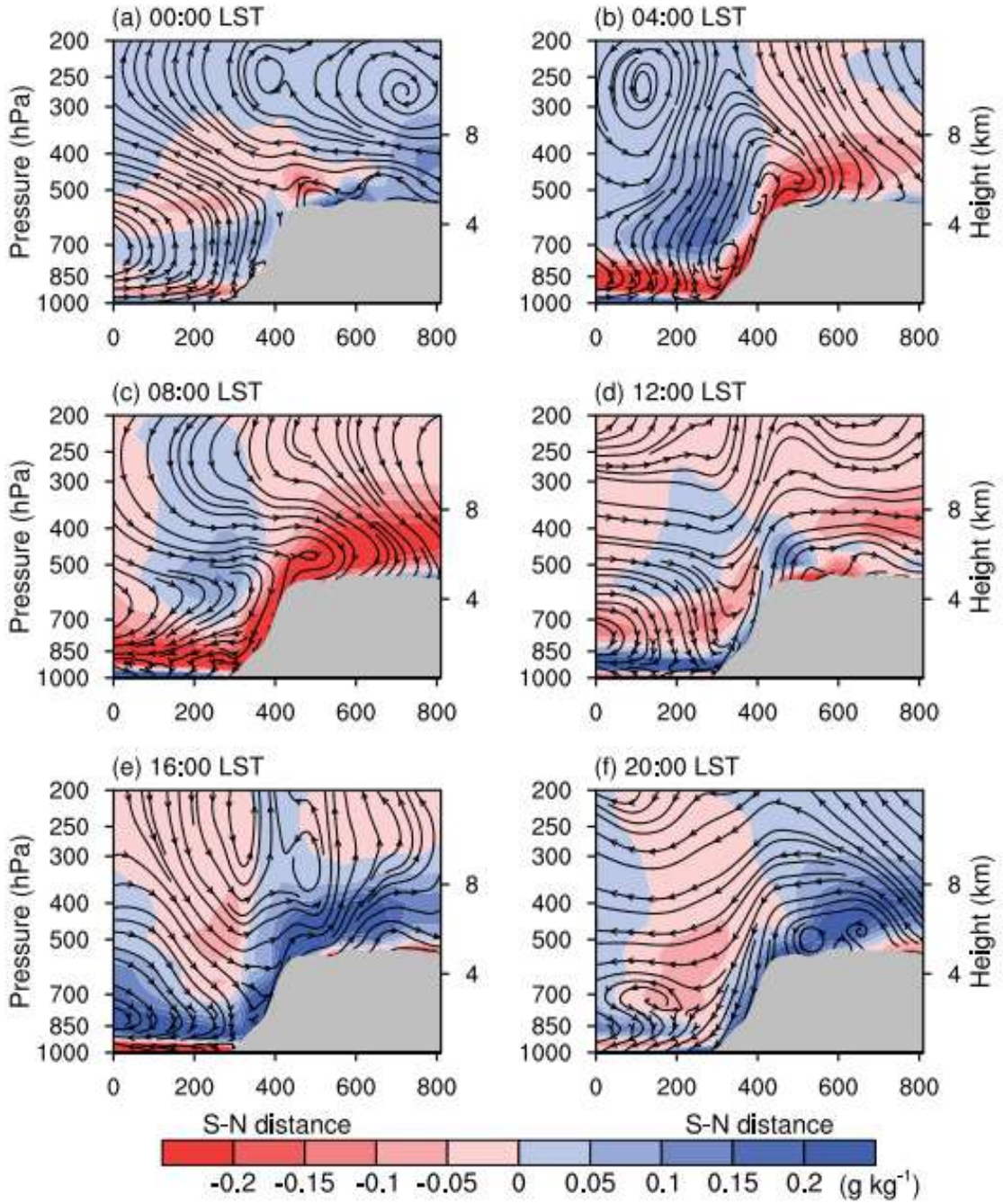

FIG. 9. South-to-north mean distributions of specific humidity anomalies overlapped with anomalous streamlines at (a) 0000, (b) 0400, (c) 0800, (d) 1200, (e) 1600, and (f) 2000 LST (UTC + 6 h).

the causes from the perspectives of the large-scale monsoon flows and the terrain circulation.

First, the horizontal distributions of 10 m wind at different local times are shown in Fig. 8. The results are consistent with Fig. 6. At 0000 to 0400 LST (Figs. 8a,b), affected by the mountain winds, the slopes are dominated by weak downslope winds; most of the foothills and plains are controlled by the BOB monsoon flow. At 0800 LST (Fig. 8c), the BOB flow becomes further strengthened owing to the zonal difference in solar heating, and the near-surface flow over the slopes is weak with the fading of mountain winds. At midday (Fig. 8d), the "heat pump" effect of the Tibetan Plateau is strong, resulting in most of the slopes and plateau being dominated by upslope flow. At 1600 LST (Fig. 8e), the zonal difference in solar heating is opposite to that of the morning: the Arabian Sea monsoon flow, which is relatively dry, strengthens and controls the west portion of the plains and foothills, and it converges with the BOB monsoon flow at the midlongitudes of the plains and foothills, which is consistent with the afternoon rainfall peak there. At 2000 LST (Fig. 8f), the near-

Brought to you by Sun Yat-Sen University | Unauthenticated | Downloaded 02/12/22 10:21 AM UTC

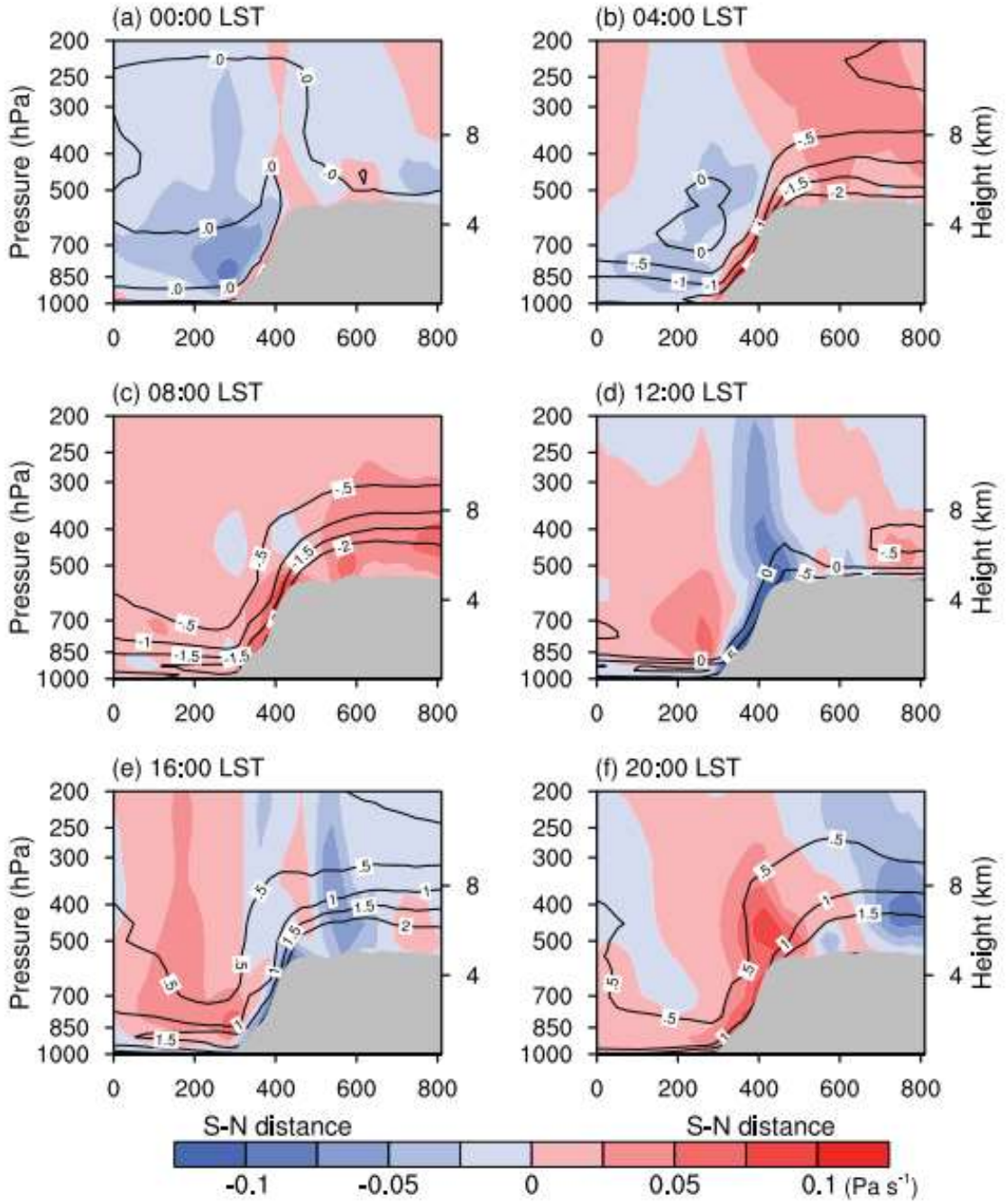

FIG. 10. As in Fig. 9, but for vertical velocity anomalies overlapped with anomalous equivalent potential temperature (units: K).

surface flow in the slopes is weak owing to the fading of the "heat pump" effect; the Arabian Sea monsoon flow also weakens without solar heating.

The South Asian summer monsoon is the most important moisture source for the Tibetan Plateau, which suggests that the diurnal rainfall peak in the plateau is associated with water vapor transport. To provide evidence for this hypothesis, the south-to-north distributions of water vapor anomalies with anomalous streamlines at different local times are given in Fig. 9. In the daytime (Figs. 9d,e), due to the "heat pump" effect of the Tibetan Plateau, the upslope flow continues to transport moisture into the plateau area, and the low-level specific humidity of the plateau rises rapidly. The moist convection forced by atmospheric buoyancy during the daytime further humidifies the middle and upper layer of the slopes and plateau. On the contrary, at night (Figs. 9a–c), due to mountain–valley wind circulations, the specific humidity of the plateau area slowly decreases owing to the lack of moisture transport and moist convection. Therefore, the total column water vapor over the plateau reaches its diurnal peak at

Brought to you by Sun Yat-Sen University | Unauthenticated | Downloaded 02/12/22 10:21 AM UTC

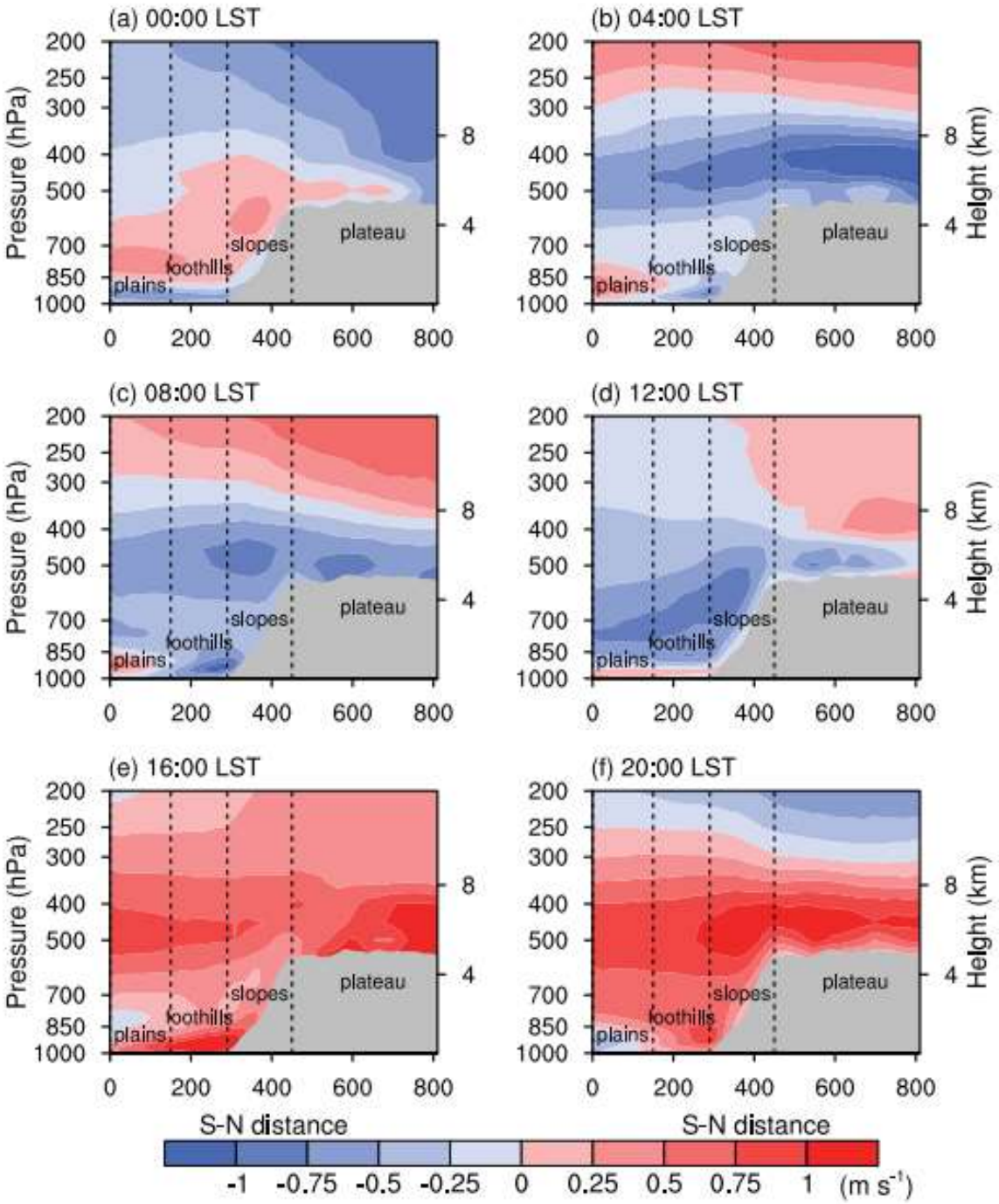

FIG. 11. As in Fig. 9, but for the average westerly circumfluent flow anomaly. The dashed lines indicate the boundaries of the study regions.

about 1600 to 2000 LST, with a near-surface specific humidity anomaly of more than 0.2 g kg^{-1} (Figs. 9e,f). In this context, isolated convection frequently occurs in plateau areas (Fu et al. 2006), which results in the diurnal rainfall peak in the plateau and in the northern slopes.

In addition, there is no obvious correlation between the diurnal cycle of precipitation and moisture over the plains and foothills, as well as the southern slopes. This is because the average total column water vapor in these regions is 10 times higher than that of the plateau and thus the subdaily moisture variation is less important. Forced by the decreased surface friction over the nocturnal atmospheric boundary layer due to surface cooling (Fig. 9a), there are strong inflow anomalies over the foothills and plains, which is a representation of the nocturnal jet (Fujinami et al. 2017, 2021).

Figure 10 shows the vertical velocity anomaly in the south-to-north cross section of the study region. From midnight to early morning (Figs. 10a,b), there is an updraft above a thin near-surface downdraft layer in the slopes and foothills. However, the anomalous equivalent potential temperature appears

Brought to you by Sun Yat-Sen University | Unauthenticated | Downloaded 02/12/22 10:21 AM UTC

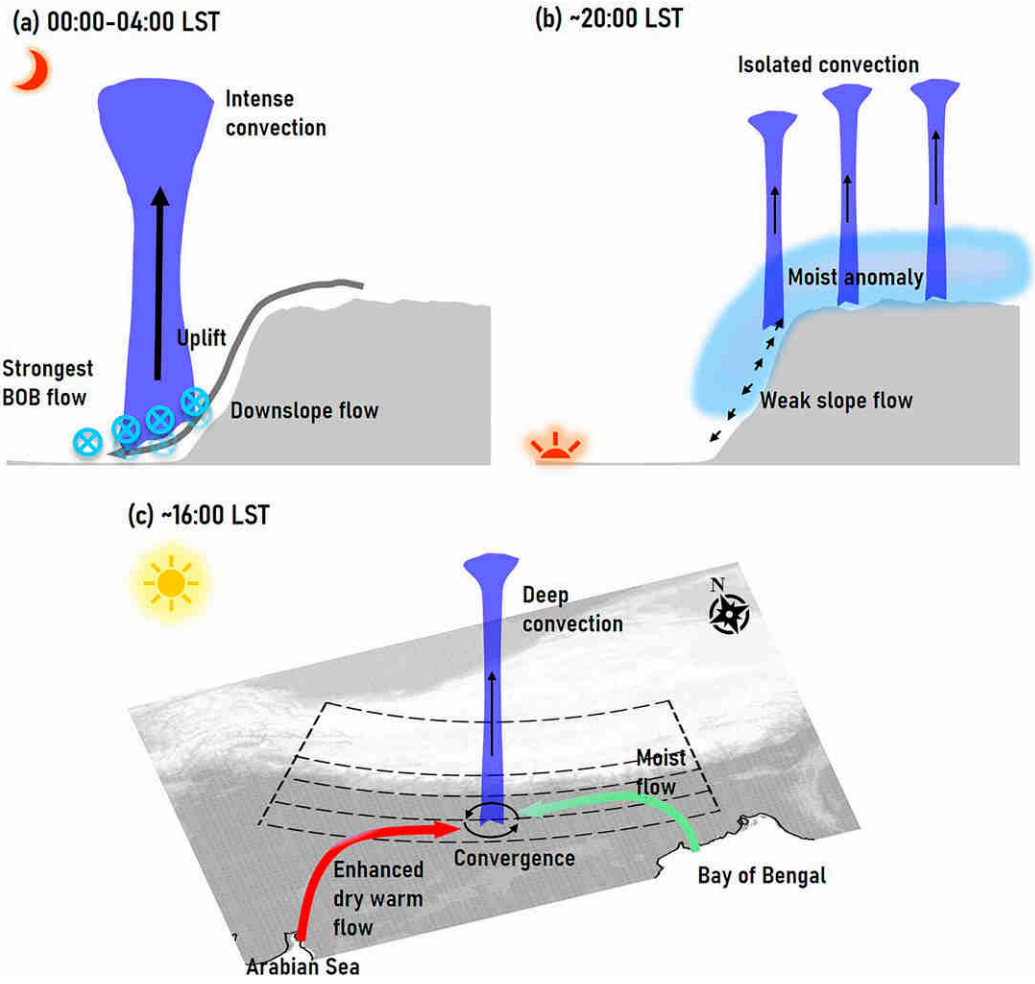

FIG. 12. (a)–(c) Conceptual diagram of the three prominent diurnal rainfall peaks over the study region during the summer monsoon season. The gray contours indicate the topography of the study regions. The arrows indicate air flows of different categories (black: local air motion; gray: downslope flow; colored: large-scale monsoon flows), and the light-blue ⊗ symbols in (a) represent inward easterly BOB monsoon flow (nocturnal jet). The deep-blue cylinders represent variant precipitation systems, while the light-blue shaded area in (b) indicates moist low-level layer.

to be increasing/stable with height, which is not conducive to the triggering of convection. Therefore, it is concluded that this updraft should be caused by the downslope winds and the nocturnal jet that forces large-scale water vapor flux convergence around the slopes and foothills (Figs. 9a and 11a). In this context, precipitation first forms over the slope region due to downslope winds and then gradually develops toward the foothills due to the water vapor flux convergence, which well reflects the southward movement of the rainfall diurnal peaks in the slopes and foothills. At 0800 LST, since both the dynamic and thermal structures are stable, the vertical velocity shows consistent descending motion in the study regions (Fig. 10c). At 1600 and 2000 LST (Figs. 10e,f), the anomalous equivalent potential temperature on the plateau shows a reduction with height, with dense contours, indicating the Tibetan Plateau is thermally unstable. There is a significant updraft in the plateau, which further promotes the occurrence of isolated convection. Similarly, there is also a strong, yet narrow, updraft associated with the upslope-flowing air just along the sloping terrain at 1200 and 1600 LST (Figs. 10d,e). On the other hand, due to the "heat pump" effect of the Tibetan Plateau, there exists a downdraft over the foothills, despite the unstable layer. The downdraft suppresses the afternoon precipitation in the foothills.

In addition, because the heating and cooling efficiency of the slope is even higher than that of the plateau, the updraft and downdraft in the slopes occurs earlier than in the plateau; at 1200 and 2000 LST (Figs. 10d,f), the air motions over the slopes and plateau are opposite.

Figure 11 shows the average south-to-north distributions of the westerly circumfluent flow anomaly. During nighttime, driven by the decreased surface friction over the stable boundary layer due to surface cooling (Figs. 10a–c), the BOB monsoon flow accelerates and is interpreted as a nocturnal jet in previous studies (Chen 2020; Fujinami et al. 2017, 2021). The

Brought to you by Sun Yat-Sen University | Unauthenticated | Downloaded 02/12/22 10:21 AM UTC

nocturnal jet is most pronounced at around 925-hPa level, which is related to the nocturnal stable boundary layer near surface. The nocturnal jet promotes precipitation over the foothills and southern slopes, and it is the main reason for the southward-moving diurnal rainfall peaks there (Fig. 7). At 1600 LST (Fig. 11e), the bottom layer of the plains presents easterly anomalous airflow, whereas the middle–upper layer presents westerly anomalous airflow, which corresponds to the intersection of the two large-scale monsoon flows (Fig. 8e). Thus, the convergence in the central plains triggers deep convection with relatively weak rainfall intensity (Houze et al. 2007).

4. Conclusions and summary

Using ERA5 hourly data and IMERG half-hourly precipitation data, we investigated the distributions of precipitation over the Himalayas under various circulation fields. We also analyzed the specific triggers for the diurnal cycles of rainfall over the Himalayas from the perspectives of the large-scale monsoon flows and terrain circulations.

As a follow-up piece of work to Chen et al. (2017), the Himalayas and surroundings were divided into the same four subregions represented by the plains, foothills, slopes, and plateau, respectively. During the summer monsoon season, the arc-shaped topographic rain belt is mainly located in the foothills and slopes. The Himalayas are affected by two large-scale monsoon flows—namely, the Arabian Sea flow and the BOB flow. When the moist BOB flow dominates, the lower layer of the foothills shows strong easterly circumfluent wind, and the rain belt is distributed relatively uniformly from east to west in the study region. Conversely, when the dry Arabian Sea monsoon flow dominates, the lower layer of the western foothills presents westerly circumfluent wind, and precipitation is concentrated on the east portion of the study area. The terrain circulations of the Himalayas mainly include the "heat pump" effect and mountain–valley wind circulations. Under the "heat pump" effect, the slopes are dominated by strong upslope flow; while under the nighttime mountain–valley wind circulation, the slopes are controlled by downslope winds. However, the precipitation intensity of the study region is strongest when the slope winds present as weak flow, which is different from normal mountain–valley precipitation. In addition, the large-scale monsoon flows are not independent of the terrain circulations, and both present significant diurnal variations. Their entangled impacts on the diurnal cycles of rainfall were studied.

Generally, the Himalayas have three prominent diurnal rainfall peaks with overlapped areas (Fig. 12). The one most closely related to the arc-shaped rain belt is the midnight-to-early-morning rainfall peak over the slopes and foothills, which presents obvious southward movement (Fig. 12a). At about 0200 LST, precipitation first occurs in the high altitudes of the slopes, affected by the downslope flow. The precipitation subsequently develops southward. In the early morning, with decreased surface friction above the nocturnal atmospheric boundary layer and the zonal differences in solar heating, the BOB moist monsoon flow reaches its daily maximum, which is known as the nocturnal jet in previous studies (Terao et al. 2006; Fujinami et al. 2017, 2021); the nocturnal jet promotes the development of intense convection over the boundary of the slopes and foothills, and the precipitation intensity reaches its diurnal peak there.

Another rainfall diurnal peak occurs in the evening over the plateau and at high altitudes of the slopes, which is linked with the moisture transport to the plateau (Fig. 12b). Affected by the "heat pump" effect, the slopes show strong upslope flow during daytime and the moisture of the plateau rises rapidly. On the other hand, the slopes show downslope flow at nighttime because of the mountain–valley wind circulation, and the specific humidity of the plateau slowly decreases. Thus, the evening is the moistest time within a day for the plateau, when isolated convection frequently occurs over the plateau and at high altitudes of the slopes because of the high total column water vapor as well as surface heating, forming the diurnal rainfall peak at about 2000 LST.

In addition, there is an afternoon rainfall peak in the plains and southern foothills (Fig. 12c). Our analysis shows that this rainfall diurnal peak is a result of the intersection of the two large-scale monsoon flows. In the afternoon, the zonal difference in solar heating promotes the hot and dry westerly monsoon flow from the Arabian Sea, whereas the moist flow from the BOB is suppressed, and the two monsoon flows thus converge in the central plains to form deep convection. However, because the moisture flux is relatively small at this moment, the precipitation intensity should be weak, as pointed out in Houze et al. (2007).

In summary, we suggest the interaction of large-scale monsoon flows and the terrain circulations to be the internal triggers of rainfall diurnal cycle over the Himalayas. The results are important for understanding orographic precipitation under monsoon environments. We summarized three major triggers for orographic precipitation over the Himalayas. Their impacts on rainfall microphysics and evolution should be further investigated using high-quality rainfall observations and model simulations.

Some of the uncertainties and limitations of the study include the following. The quality of ERA5 data, especially near-surface wind at 10 m above ground level, highly depends on the numerical model due to the lack of observations around the Himalayas and Tibetan Plateau. Although Huai et al. (2021) suggested that ERA5 outperforms the other reanalysis datasets over the Tibetan Plateau, the near-surface wind speed may still be slightly underestimated by ERA5. Future use of a better environment dataset, such as observations from the Aeolus mission, will add robustness to the results presented here.

Acknowledgments. The authors greatly appreciate the thoughtful comments and suggestions of the editor and other three anonymous reviewers. This work was supported by the Guangdong Major Project of Basic and Applied Basic Research (Grant 2020B0301030004), National Natural Science Foundation of China (Grants 91837310, 41705011, 42075004, 42005062, and 42105068), and Natural Science Foundation of Guangdong Province of China (Grant 2021A1515011404). The authors declare no conflict of interests.

Brought to you by Sun Yat-Sen University | Unauthenticated | Downloaded 02/12/22 10:21 AM UTC

REFERENCES

Barros, A. P., M. Joshi, J. Putkonen, and D. W. Burbank, 2000: A study of the 1999 monsoon rainfall in a mountainous region in central Nepal using TRMM products and rain gauge observations. *Geophys. Res. Lett.*, **27**, 3683–3686, https://doi.org/10.1029/2000GL011827.

Bhatt, B. C., and K. Nakamura, 2005: Characteristics of monsoon rainfall around the Himalayas revealed by TRMM Precipitation Radar. *Mon. Wea. Rev.*, **133**, 149–165, https://doi.org/10.1175/MWR-2846.1.

Bookhagen, B., and D. W. Burbank, 2006: Topography, relief, and TRMM-derived rainfall variations along the Himalaya. *Geophys. Res. Lett.*, **33**, L08405, https://doi.org/10.1029/2006GL026037.

Boos, W. R., and Z. Kuang, 2010: Dominant control of the South Asian monsoon by orographic insulation versus plateau heating. *Nature*, **463**, 218–222, https://doi.org/10.1038/nature08707.

Chen, G., 2020: Diurnal cycle of the Asian summer monsoon: Air pump of the second kind. *J. Climate*, **33**, 1747–1775, https://doi.org/10.1175/JCLI-D-19-0210.1.

——, R. Lan, W. Zeng, H. Pan, and W. Li, 2018: Diurnal variations of rainfall in surface and satellite observations at the monsoon coast (South China). *J. Climate*, **31**, 1703–1724, https://doi.org/10.1175/JCLI-D-17-0373.1.

Chen, Y., Y. Fu, T. Xian, and X. Pan, 2017: Characteristics of cloud cluster over the steep southern slopes of the Himalayas observed by CloudSat. *Int. J. Climatol.*, **37**, 4043–4052, https://doi.org/10.1002/joc.4992.

Egger, J., S. Bajrachaya, U. Egger, R. Heinrich, J. Reuder, P. Shayka, H. Wendt, and V. Wirth, 2000: Diurnal winds in the Himalayan Kali Gandaki Valley. Part I: Observations. *Mon. Wea. Rev.*, **128**, 1106–1122, https://doi.org/10.1175/1520-0493(2000)128<1106:DWITHK>2.0.CO;2.

Fu, Y., G. S. Liu, G. X. Wu, R. C. Yu, Y. P. Xu, Y. Wang, R. Li, and Q. Liu, 2006: Tower mast of precipitation over the central Tibetan Plateau summer. *Geophys. Res. Lett.*, **33**, L05802, https://doi.org/10.1029/2005GL024713.

——, and Coauthors, 2018: Precipitation characteristics over the steep slope of the Himalayas in rainy season observed by TRMM PR and VIRS. *Climate Dyn.*, **51**, 1971–1989, https://doi.org/10.1007/s00382-017-3992-3.

Fujinami, H., T. Sato, H. Kanamori, and F. Murata, 2017: Contrasting features of monsoon precipitation around the Meghalaya Plateau under westerly and easterly regimes. *J. Geophys. Res. Atmos.*, **122**, 9591–9610, https://doi.org/10.1002/2016JD026116.

——, K. Fujita, N. Takahashi, T. Sato, H. Kanamori, S. Sunako, and R. B. Kayastha, 2021: Twice-daily monsoon precipitation maxima in the Himalayas driven by land surface effects. *J. Geophys. Res. Atmos.*, **126**, e2020JD034255, https://doi.org/10.1029/2020JD034255.

Gadgil, S., and S. Sajani, 1998: Monsoon precipitation in the AMIP runs. *Climate Dyn.*, **14**, 659–689, https://doi.org/10.1007/s003820050248.

Hersbach, H., and Coauthors, 2020: The ERA5 global reanalysis. *Quart. J. Roy. Meteor. Soc.*, **146**, 1999–2049, https://doi.org/10.1002/qj.3803.

Hirose, M., and K. Nakamura, 2005: Spatial and diurnal variation of precipitation systems over Asia observed by the TRMM Precipitation Radar. *J. Geophys. Res.*, **110**, D05106, https://doi.org/10.1029/2004JD004815.

Houze, R. A., Jr., D. C. Wilton, and B. F. Smull, 2007: Monsoon convection in the Himalayan region as seen by the TRMM Precipitation Radar. *Quart. J. Roy. Meteor. Soc.*, **133**, 1389–1411, https://doi.org/10.1002/qj.106.

Huai, B., J. Wang, W. Sun, Y. Wang, and W. Zhang, 2021: Evaluation of the near-surface climate of the recent global atmospheric reanalysis for Qilian Mountains, Qinghai-Tibet Plateau. *Atmos. Res.*, **250**, 105401, https://doi.org/10.1016/j.atmosres.2020.105401.

Huffman, G. J., and Coauthors, 2019: NASA Global Precipitation Measurement (GPM) Integrated Multi-satellite Retrievals for GPM (IMERG). NASA Algorithm Theoretical Basis Doc., version 06, 38 pp., https://gpm.nasa.gov/sites/default/files/2019-05/IMERG_ATBD_V06.pdf.

——, D. T. Bolvin, E. J. Nelkin, E. F. Stocker, and J. Tan, 2020: V06 IMERG release notes. NASA GPM Doc., 15 pp., https://docserver.gesdisc.eosdis.nasa.gov/public/project/GPM/IMERG_V06_release_notes.pdf.

Johnson, R. H., 2011: Diurnal cycle of monsoon convection. *The Global Monsoon System: Research and Forecast*, World Scientific, 257–276.

Kingsmill, D. E., P. J. Neiman, and A. B. White, 2016: Microphysics regime impacts on the relationship between orographic rain and orographic forcing in the coastal mountains of Northern California. *J. Hydrometeor.*, **17**, 2905–2922, https://doi.org/10.1175/JHM-D-16-0103.1.

Kumar, S., Y. Vidal, A. S. Moya-Álvarez, and D. Martínez-Castro, 2019: Effect of the surface wind flow and topography on precipitating cloud systems over the Andes and associated Amazon basin: GPM observations. *Atmos. Res.*, **225**, 193–208, https://doi.org/10.1016/j.atmosres.2019.03.027.

Nesbitt, S. W., and E. J. Zipser, 2003: The diurnal cycle of rainfall and convective intensity according to three years of TRMM measurements. *J. Climate*, **16**, 1456–1475, https://doi.org/10.1175/1520-0442-16.10.1456.

Ouyang, L., K. Yang, H. Lu, Y. Chen, X. Zhou, and Y. Wang, 2020: Ground-based observations reveal unique valley precipitation patterns in the central Himalaya. *J. Geophys. Res. Atmos.*, **125**, e2019JD031502, https://doi.org/10.1029/2019JD031502.

Pan, X., Y. Fu, S. Yang, Y. Gong, and D. Li, 2021: Diurnal variations of precipitation over the steep slopes of the Himalayas observed by TRMM PR and VIRS. *Adv. Atmos. Sci.*, **38**, 641–660, https://doi.org/10.1007/s00376-020-0246-9.

Pang, H., and Coauthors, 2012: Atmospheric circulation change in the central Himalayas indicated by a high-resolution ice core deuterium excess record. *Climate Res.*, **53**, 1–12, https://doi.org/10.3354/cr01090.

Rasmussen, K. L., and R. A. Houze Jr., 2012: A flash-flooding storm at the steep edge of high terrain disaster in the Himalayas. *Bull. Amer. Meteor. Soc.*, **93**, 1713–1724, https://doi.org/10.1175/BAMS-D-11-00236.1.

Sahany, S., V. Venugopal, and R. S. Nanjundiah, 2010: Diurnal-scale signatures of monsoon rainfall over the Indian region from TRMM satellite observations. *J. Geophys. Res.*, **115**, D02103, https://doi.org/10.1029/2009JD012644.

Shrestha, D., P. Singh, and K. Nakamura, 2012: Spatiotemporal variation of rainfall over the central Himalayan region revealed by TRMM Precipitation Radar. *J. Geophys. Res.*, **117**, D22106, https://doi.org/10.1029/2012JD018140.

Tan, J., G. J. Huffman, D. T. Bolvin, and E. J. Nelkin, 2019: Diurnal cycle of IMERG v06 precipitation. *Geophys. Res. Lett.*, **46**, 13 584–13 592, https://doi.org/10.1029/2019GL085395.

Brought to you by Sun Yat-Sen University | Unauthenticated | Downloaded 02/12/22 10:21 AM UTC

Terao, T., M. N. Islam, T. Hayashi, and T. Oka, 2006: Nocturnal jet and its effects on early morning rainfall peak over northeastern Bangladesh during the summer monsoon season. *Geophys. Res. Lett.*, **33**, L18806, https://doi.org/10.1029/2006GL026156.

Wang, L., H. Hu, and X. Yang, 2019: The atmospheric responses to the intensity variability of subtropical front in the wintertime North Pacific. *Climate Dyn.*, **52**, 5623–5639, https://doi.org/10.1007/s00382-018-4468-9.

Wang, Z., A. Duan, G. Wu, and S. Yang, 2016: Mechanism for occurrence of precipitation over the southern slope of the Tibetan Plateau without local surface heating. *Int. J. Climatol.*, **36**, 4164–4171, https://doi.org/10.1002/joc.4609.

Wu, G., and Coauthors, 2007: The influence of mechanical and thermal forcing by the Tibetan Plateau on Asian climate. *J. Hydrometeor.*, **8**, 770–789, https://doi.org/10.1175/JHM609.1.

——, Y. Liu, B. He, Q. Bao, A. Duan, and F. Jin, 2012: Thermal controls on the Asian summer monsoon. *Sci. Rep.*, **2**, 404, https://doi.org/10.1038/srep00404.

Xue, M., X. Luo, K. Zhu, Z. Sun, and J. Fei, 2018: The controlling role of boundary layer inertial oscillations in meiyu frontal precipitation and its diurnal cycles over China. *J. Geophys. Res. Atmos.*, **123**, 5090–5115, https://doi.org/10.1029/2018JD028368.

Yu, R., T. Zhou, A. Xiong, Y. Zhu, and J. Li, 2007: Diurnal variations of summer precipitation over contiguous China. *Geophys. Res. Lett.*, **34**, L01704, https://doi.org/10.1029/2006GL028129.

——, J. Li, H. Chen, and W. Yuan, 2014: Progress in studies of the precipitation diurnal variation over contiguous China. *J. Meteor. Res.*, **28**, 877–902, https://doi.org/10.1007/s13351-014-3272-7.

Yuan, W., R. Yu, M. Zhang, W. Lin, H. Chen, and J. Li, 2012: Regimes of diurnal variation of summer rainfall over subtropical East Asia. *J. Climate*, **25**, 3307–3320, https://doi.org/10.1175/JCLI-D-11-00288.1.

Zhang, A., Y. Fu, Y. Chen, G. Liu, and X. Zhang, 2018: Impact of the surface wind flow on precipitation characteristics over the southern Himalayas: GPM observations. *Atmos. Res.*, **202**, 10–22, https://doi.org/10.1016/j.atmosres.2017.11.001.

——, Y. L. Chen, S. N. Zhou, C. G. Cui, R. Wan, and Y. F. Fu, 2020: Diurnal variation of meiyu rainfall in the Yangtze Plain during atypical meiyu years. *J. Geophys. Res. Atmos.*, **125**, e2019JD031742, https://doi.org/10.1029/2019JD031742.

Brought to you by Sun Yat-Sen University | Unauthenticated | Downloaded 02/12/22 10:21 AM UTC